The Astrophysical Journal, 695:666–678, 2009 April 10 doi:10.1088/0004-637X/695/1/666

THE PHOSPHORUS, SULFUR, ARGON, AND CALCIUM ISOTOPIC COMPOSITION OF THE GALACTIC COSMIC RAY SOURCE

R. C. Ogliore[1,6], E. C. Stone[1], R. A. Leske[1], R. A. Mewaldt[1], M. E. Wiedenbeck[2], W. R. Binns[3], M. H. Israel[3], T. T. von Rosenvinge[4], G. A. de Nolfo[4], and I. V. Moskalenko[5]
[1] California Institute of Technology, Pasadena, CA 91125, USA; ogliore@srl.caltech.edu
[2] Jet Propulsion Laboratory, California Institute of Technology, Pasadena, CA 91109, USA
[3] Washington University, St. Louis, MO 63130, USA
[4] NASA/Goddard Space Flight Center, Greenbelt, MD 20771,USA
[5] HEPL & KIPAC, Stanford University, Stanford, CA 94305, USA
Received 2008 November 18; accepted 2009 January 13; published 2009 April 1

ABSTRACT

Galactic cosmic ray (GCR) measurements of the phosphorus, sulfur, argon, and calcium isotopes made by the Cosmic Ray Isotope Spectrometer aboard the *Advanced Composition Explorer* are reported over the energy range from ∼100 to ∼400 MeV nucleon^{-1}. The propagation of cosmic rays through the Galaxy and heliosphere is modeled with constraints imposed by measurements. Isotopic source abundance ratios ^{31}P/^{32}S, ^{34}S/^{32}S, ^{38}Ar/^{36}Ar, and ^{44}Ca/^{40}Ca are deduced. The derived ^{31}P/^{32}S ratio is 2.34 ± 0.34 times larger than the solar system value, lending further credence to the suggestion that refractory elements are enriched in the GCRs due to the sputtering of ions off grains in the cores of superbubbles. By determining the GCR source abundances of argon (a noble gas) and calcium (a refractory), it is determined that material in grains is accelerated to GCR energies a factor of 6.4 ± 0.3 more efficiently than gas-phase material in this charge range. With this information, the dust fraction of phosphorus and sulfur in the interstellar material that is mixed with stellar ejecta to form the GCR seed material is found to be consistent with astronomical observations.

Key words: cosmic rays – Galaxy: abundances – ISM: abundances – ISM: bubbles – supernovae: general

1. INTRODUCTION

The galactic cosmic rays (GCRs) detected near Earth provide a unique perspective on astrophysical processes because they are the only high-energy, extrasolar material that is directly sampled. The elemental and isotopic GCR composition, measured with high precision in recent years by satellite experiments (Engelmann et al. 1990; George et al. 2009; Wiedenbeck et al. 2001b, 2007a), is similar to solar system material for many species but differs significantly for others. Any theory for the proposed GCR source environment and acceleration mechanism must be consistent with modern measurements over the ensemble of GCR species.

When the abundances of elements in the GCRs are compared with those of elements in the solar system, refractory elements are significantly enhanced relative to those of volatile elements. A proposed mechanism for this enhancement is the preferential acceleration of refractory elements due to injection by sputtering off preaccelerated, high-velocity refractory grains through collisions with ambient gas in the GCR acceleration environment (Meyer et al. 1997). These atoms are later accelerated to GCR energies. The GCR elemental abundances have been shown to be ordered by the observed depletion of those elements out of the gas phase (and onto grains) in the interstellar medium (ISM) (Tarafdar & Apparao 1981): the elements that exist mostly in grains in the ISM are more abundant in the GCRs. In addition, first ionization potential (FIP) is inversely correlated with condensation temperature for most elements seen in the GCRs. Therefore, the observed GCR enrichment could be controlled by FIP as was first thought (Cassé & Goret 1978; Meyer 1985) instead of an element's propensity for condensing into grains. The physical mechanism for preferential acceleration of low-FIP species to GCR energies involves, for most models (e.g., Meyer 1985), a two-step acceleration at different locations. To determine whether the controlling parameter of GCR fractionation is FIP or volatility, precise measurements of elements that break the FIP–volatility correlation are needed. Phosphorus and sulfur have very similar FIPs (∼11 eV), but sulfur condenses at ∼700 K whereas phosphorus condenses at ∼1250 K (Lodders 2003). The GCR source ratio of phosphorus to sulfur, when compared to the bulk solar system ratio (as determined from meteoritic and photospheric abundances by Lodders 2003), can help distinguish whether FIP or volatility is responsible for the observed GCR fractionation (Meyer et al. 1997; George et al. 2001).

It has been argued that the acceleration site of GCRs is likely to be the hot, tenuous cores of superbubbles produced by OB associations (Higdon et al. 1998; Higdon & Lingenfelter 2003). Dust grains and gas from the interstellar medium mix with ejecta from supernovae and outflow from massive stars that evolve into Wolf–Rayet (W–R) stars inside the superbubble (Lingenfelter & Higdon 2007). Supernova shocks accelerate the mixture of older ISM material and freshly synthesized ejecta from core-collapse Type Ib/c and Type II supernovae, as well as the ejecta from W–R stars and some Type Ia supernova ejecta. Certain physical parameters of this situation should be manifest in the composition of the GCRs. First ionization potential should have little reference to the GCR acceleration process in the nearly fully ionized superbubble interior, so the GCR P/S ratio should be larger than that found in solar system material if the GCR fractionation is controlled by volatility. If the isotopic composition of the ISM material is different from that of the stellar ejecta, the amount of mixing between these components should be seen in the composition of the GCRs accelerated from that mix. As described by Ellison et al. (1997), supernova shocks

[6] Current address: University of California, Berkeley-Space Sciences Laboratory, 7 Gauss Way, Berkeley, CA 94720-7450, USA; ogliore@ssl.berkeley.edu.

preferentially accelerate higher rigidity particles. Therefore, the material present in old ISM grains and supernova condensate grains is accelerated to ∼0.1 MeV nucleon^{-1} more efficiently than gas-phase material because these charged grains are seen as very high rigidity particles by the shock. After sputtering, the ions are accelerated further by the shock, resulting in a GCR enhancement of matter that is condensed into grains in the GCR seed material.

The mixture of material inside superbubbles has been estimated to be ∼20% ejecta and ∼80% material from the surrounding ISM. This mixing was calculated by Higdon & Lingenfelter (2003) using the measurements by Binns et al. (2000) of the GCR neon isotopes at Earth and then determining the cosmic ray source ^{22}Ne/^{20}Ne ratio, which is about five times larger than the solar system value. The 80/20 mixing is consistent with other GCR isotope ratios that are affected by the W–R component in the GCR source: ^{58}Fe/^{56}Fe and ^{12}C/^{16}O (Binns et al. 2005). The element ratios Si/Fe, C/Fe, and O/Fe in the GCRs as well as the Be/Fe ratio in old halo stars have been shown to be consistent with approximately 80/20 mixing of fresh supernova ejecta and old interstellar medium (Lingenfelter & Higdon 2007).

In this paper, we present measurements of the isotopes of phosphorus, sulfur, argon, and calcium made by the Cosmic Ray Isotope Spectrometer (CRIS; Stone et al. 1998) aboard the *Advanced Composition Explorer* (*ACE*). From these measurements, the isotopic source abundances are derived using purely secondary GCR species as tracers of the secondary production (Stone & Wiedenbeck 1979). The GCR species investigated in this paper cover the range from highly volatile species that exist solely in the gas phase (argon) to refractory isotopes that readily condense into grains (calcium). From the GCR source abundances of these isotopes, we obtain insight into the grain and gas composition of the cosmic ray source material.

2. MEASUREMENTS

The CRIS instrument aboard *ACE* measures the elemental and isotopic composition of GCRs by making multiple measurements of a particle's dE/dx and its total energy (Stone et al. 1998). The sensor system is composed of four stacks of silicon solid-state detectors (sometimes with two detector wafers electronically connected to make a single effective detector) and a scintillating fiber hodoscope to measure the particle's trajectory through the detector stack.

The CRIS measurements used in this work were obtained between 1997 August 28 and 1999 August 17, a period of low solar modulation. This data set was selected to have incoming trajectories less than 50° from the normal to the detector surface because the mass resolution of the sensor system degrades at larger angles due to multiple Coulomb scattering (Stone et al. 1998). The mass resolution as a function of incident angle for Range 7 sulfur (sulfur nuclei stopping in the seventh detector in the stack of silicon detectors) is shown in Figure 1. Particles that deposited energy in the last detector in the detector stack or had trajectories and measured energies consistent with having exited through the sides of the instrument without stopping in a detector, as well as those that only deposited energy in the first detector, were eliminated. The remaining particles are those that stopped in the detector stack and penetrated at least two detectors, a requirement for calculating a particle's charge and mass. Charge collection 50–60 μm from the detector surface, known as the dead layer, is inefficient, and particles that deposit only a small amount of energy in the stopping detector are not identified accurately during data reduction. To further improve the resolution of the data set, particles stopping near these dead layers (specifically, in the top 150 μm of the top detector wafer and bottom 500 μm of the bottom detector wafer) were removed. Particles that fragmented in the detector stack were also discarded from the data set by requiring consistency among the multiple calculations of particle charge Z. In addition, a consistent trajectory measured by the scintillating optical fiber trajectory (SOFT) hodoscope is required of each incoming particle, and it must pass more than 500 μm away from the edge of the active area. Particles must pass more than 500 μm from the edge of the silicon detectors.

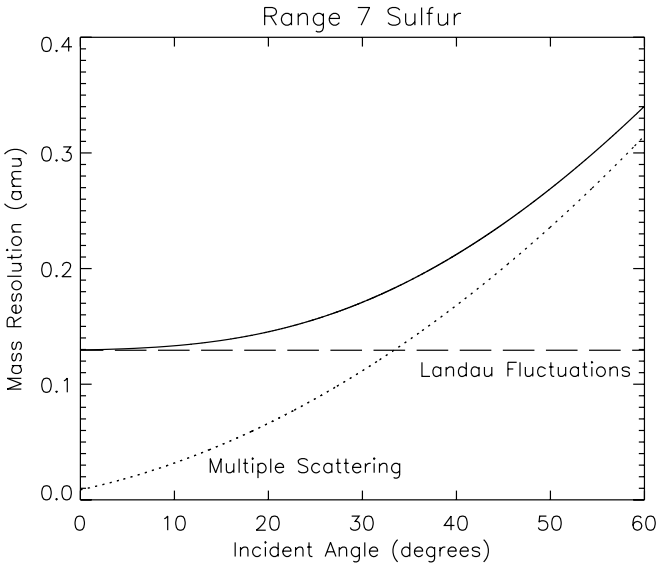

Figure 1. Two dominant contributions to mass resolution in the CRIS data are from Landau fluctuations (energy loss fluctuations in the dE detector) and multiple Coulomb scattering (deflections in the particle's trajectory caused by Coulomb interactions between the incident charged particle and the detector material). The multiple scattering contribution, shown here as a dotted line calculated from theory (Stone et al. 1998) for Range 7 sulfur in CRIS, increases with increasing angle, where Landau fluctuations (dashed line) remain constant as the angle of the incident particle increases. The solid line shows the total mass resolution, the quadrature sum of these two components.

The particles with trajectories less than 25° from the detector normal were analyzed separately from particles with trajectories between 25° and 50°. Phosphorus, sulfur, argon, and calcium mass histograms are shown in Figure 2 for CRIS range 4 with trajectories less than 25°. The abundances of the isotopes for events with trajectories between 25° and 50° were determined with reasonable precision as shown in Figure 3. The large-angle isotope abundances agreed, to within statistical uncertainties, with the small-angle data so the two data sets were combined to yield approximately a factor of 2 increase in statistics over the small-angle data. The histogrammed counts of an element measured by the CRIS instrument over this time period results in a Gaussian-like bell curve for each isotope, where the width of the Gaussian depends, in part, on the incident angle of the incoming particle. The dependence of the mass resolution as a function of incident angle was determined for each element. This dependence was then used in a multiple-Gaussian maximum likelihood technique to fit the data and obtain abundances for each isotope, with the mean mass of the isotope also taken as a free parameter in the fit. Table 1 shows the fit values for the abundances and masses of each isotope and associated 1σ uncertainties. The maximum likelihood fits to the data are shown as the solid curves in Figures 2 and 3.

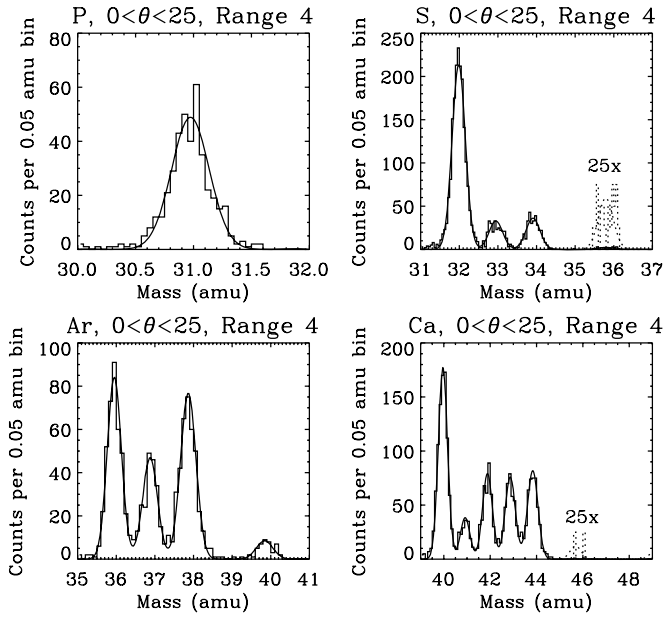

Figure 2. CRIS Range 4 mass histograms for phosphorus, sulfur, argon, and calcium with angles of incidence less than 25°. The solid line is a maximum likelihood fit to the data, from which isotopic abundances are determined. The dotted lines show rare isotope abundances and fits multiplied by 25.

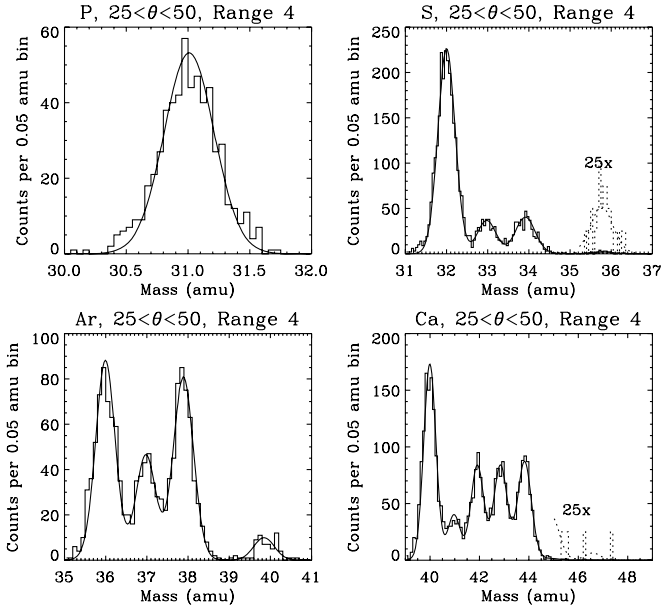

Figure 3. CRIS Range 4 mass histograms for phosphorus, sulfur, argon, and calcium with angles of incidence greater than 25° and less than 50°. The solid line is a maximum likelihood fit to the data, from which isotopic abundances are determined. The dotted lines show rare isotope abundances and fits multiplied by 25.

Isotope counts for each detector range are given in Tables 2–5. The counts were calculated by summing the maximum likelihood fits of the small-angle and large-angle data and applying corrections for spallation losses and efficiency of the SOFT hodoscope. The median energy for each element and CRIS detector range is also given. To obtain isotope ratios for the same energy interval, a correction must be applied to the counts of an isotope in a given CRIS range to account for the slightly different energy interval and spectral shape of the two

Table 1
Maximum Likelihood Parameters and Uncertainties

Isotope	Acceptance Angle	Range	N	σ_N	M	σ_M (10^{-2})
^{31}P	0° –25°	2	229	15	31.01	0.07
^{31}P	0° –25°	3	492	22	31.03	0.03
^{31}P	0° –25°	4	400	20	30.97	0.04
^{31}P	0° –25°	5	338	18	30.96	0.05
^{31}P	0° –25°	6	305	17	30.97	0.05
^{31}P	0° –25°	7	234	15	30.98	0.07
^{31}P	0° –25°	8	238	15	30.98	0.07
^{31}P	25° –50°	2	411	20	31.01	0.05
^{31}P	25° –50°	3	787	28	31.02	0.03
^{31}P	25° –50°	4	543	23	31.01	0.04
^{31}P	25° –50°	5	395	20	31.00	0.05
^{31}P	25° –50°	6	260	16	31.01	0.08
^{31}P	25° –50°	7	217	15	30.99	0.10
^{31}P	25° –50°	8	204	14	30.99	0.10
^{32}S	0° –25°	2	1215	35	32.00	0.56
^{32}S	0° –25°	3	2110	46	32.00	0.43
^{32}S	0° –25°	4	1834	43	31.99	0.46
^{32}S	0° –25°	5	1465	38	31.97	0.50
^{32}S	0° –25°	6	1246	35	31.97	0.55
^{32}S	0° –25°	7	1080	33	31.97	0.57
^{32}S	0° –25°	8	981	31	31.97	0.59
^{32}S	25° –50°	2	2195	47	32.02	0.53
^{32}S	25° –50°	3	3357	58	32.00	0.42
^{32}S	25° –50°	4	2375	49	32.00	0.50
^{32}S	25° –50°	5	1678	41	31.98	0.61
^{32}S	25° –50°	6	1116	34	31.98	0.77
^{32}S	25° –50°	7	817	29	31.98	0.89
^{32}S	25° –50°	8	677	26	31.98	0.99
^{33}S	0° –25°	2	169	13	32.95	1.81
^{33}S	0° –25°	3	385	20	32.94	1.10
^{33}S	0° –25°	4	292	17	32.95	1.17
^{33}S	0° –25°	5	281	17	32.91	1.23
^{33}S	0° –25°	6	243	16	32.92	1.27
^{33}S	0° –25°	7	229	15	32.93	1.21
^{33}S	0° –25°	8	210	15	32.94	1.27
^{33}S	25° –50°	2	337	20	32.93	1.79
^{33}S	25° –50°	3	539	25	32.93	1.33
^{33}S	25° –50°	4	416	22	32.97	1.54
^{33}S	25° –50°	5	338	20	32.93	1.73
^{33}S	25° –50°	6	248	17	32.95	2.04
^{33}S	25° –50°	7	190	15	32.94	2.20
^{33}S	25° –50°	8	139	13	32.89	2.91
^{34}S	0° –25°	2	235	15	33.87	1.44
^{34}S	0° –25°	3	429	21	33.90	1.00
^{34}S	0° –25°	4	330	18	33.91	1.02
^{34}S	0° –25°	5	347	19	33.90	1.03
^{34}S	0° –25°	6	294	17	33.92	1.05
^{34}S	0° –25°	7	245	16	33.92	1.03
^{34}S	0° –25°	8	276	17	33.91	1.25
^{34}S	25° –50°	2	425	21	33.86	1.33
^{34}S	25° –50°	3	726	27	33.92	0.94
^{34}S	25° –50°	4	492	23	33.91	1.23
^{34}S	25° –50°	5	385	20	33.92	1.39
^{34}S	25° –50°	6	275	17	33.92	1.64
^{34}S	25° –50°	7	234	16	33.91	1.66
^{34}S	25° –50°	8	165	13	33.87	2.01
^{36}S	0° –25°	2	7	3	35.85	9.73
^{36}S	0° –25°	3	24	5	35.80	4.20
^{36}S	0° –25°	4	23	5	35.79	3.63
^{36}S	0° –25°	5	20	4	35.85	4.16
^{36}S	0° –25°	6	20	4	35.81	3.51
^{36}S	0° –25°	7	7	3	35.82	5.32
^{36}S	0° –25°	8	16	4	35.71	12.06
^{36}S	25° –50°	2	25	5	35.78	5.20
^{36}S	25° –50°	3	28	5	35.66	4.64

Table 1
(Continued)

Isotope	Acceptance Angle	Range	N	σ_N	M	σ_M (10^{-2})
^{36}S	25° –50°	4	29	5	35.77	4.85
^{36}S	25° –50°	5	31	6	35.79	4.36
^{36}S	25° –50°	6	10	3	35.87	7.74
^{36}S	25° –50°	7	11	3	35.84	7.10
^{36}S	25° –50°	8	9	3	35.88	7.69
^{36}Ar	0° –25°	2	273	17	35.98	1.14
^{36}Ar	0° –25°	3	476	22	35.97	0.90
^{36}Ar	0° –25°	4	386	20	35.95	0.96
^{36}Ar	0° –25°	5	327	18	35.94	1.04
^{36}Ar	0° –25°	6	279	17	35.91	1.09
^{36}Ar	0° –25°	7	243	16	35.93	1.19
^{36}Ar	0° –25°	8	222	15	35.95	1.18
^{36}Ar	25° –50°	2	488	22	36.01	1.00
^{36}Ar	25° –50°	3	709	27	36.00	0.90
^{36}Ar	25° –50°	4	527	23	35.99	1.10
^{36}Ar	25° –50°	5	393	20	35.96	1.27
^{36}Ar	25° –50°	6	252	16	35.95	1.45
^{36}Ar	25° –50°	7	214	15	35.96	1.63
^{36}Ar	25° –50°	8	160	13	35.95	2.03
^{38}Ar	0° –25°	2	216	15	37.83	1.42
^{38}Ar	0° –25°	3	490	22	37.87	1.00
^{38}Ar	0° –25°	4	386	20	37.86	1.05
^{38}Ar	0° –25°	5	358	19	37.87	1.10
^{38}Ar	0° –25°	6	274	17	37.85	1.23
^{38}Ar	0° –25°	7	217	15	37.85	1.39
^{38}Ar	0° –25°	8	255	16	37.87	1.28
^{38}Ar	25° –50°	2	420	21	37.88	1.32
^{38}Ar	25° –50°	3	806	29	37.86	1.03
^{38}Ar	25° –50°	4	497	23	37.89	1.23
^{38}Ar	25° –50°	5	410	21	37.88	1.37
^{38}Ar	25° –50°	6	322	18	37.89	1.56
^{38}Ar	25° –50°	7	213	15	37.89	1.99
^{38}Ar	25° –50°	8	175	14	37.89	2.09
^{40}Ca	0° –25°	2	586	24	40.00	0.82
^{40}Ca	0° –25°	3	1096	33	39.98	0.66
^{40}Ca	0° –25°	4	882	30	39.96	0.68
^{40}Ca	0° –25°	5	693	27	39.96	0.84
^{40}Ca	0° –25°	6	571	24	39.95	0.81
^{40}Ca	0° –25°	7	454	21	39.96	0.89
^{40}Ca	0° –25°	8	399	20	39.96	1.05
^{40}Ca	25° –50°	2	1053	33	40.03	0.77
^{40}Ca	25° –50°	3	1662	42	40.01	0.63
^{40}Ca	25° –50°	4	1069	33	39.99	0.82
^{40}Ca	25° –50°	5	727	28	40.00	1.02
^{40}Ca	25° –50°	6	505	24	39.98	1.26
^{40}Ca	25° –50°	7	402	21	39.99	1.37
^{40}Ca	25° –50°	8	283	18	39.98	1.76
^{41}Ca	0° –25°	2	114	11	40.81	2.51
^{41}Ca	0° –25°	3	235	16	40.90	1.77
^{41}Ca	0° –25°	4	197	15	40.92	1.73
^{41}Ca	0° –25°	5	183	14	40.89	1.94
^{41}Ca	0° –25°	6	150	13	40.89	1.93
^{41}Ca	0° –25°	7	136	12	40.93	1.90
^{41}Ca	0° –25°	8	113	11	40.94	2.32
^{41}Ca	25° –50°	2	230	17	40.88	2.33
^{41}Ca	25° –50°	3	366	21	40.95	2.01
^{41}Ca	25° –50°	4	255	18	40.97	2.49
^{41}Ca	25° –50°	5	192	16	40.92	2.99
^{41}Ca	25° –50°	6	142	14	40.90	3.71
^{41}Ca	25° –50°	7	95	11	40.90	4.16
^{41}Ca	25° –50°	8	92	11	40.93	4.53
^{42}Ca	0° –25°	2	251	16	41.81	1.53
^{42}Ca	0° –25°	3	515	23	41.87	1.07

Table 1
(Continued)

Isotope	Acceptance Angle	Range	N	σ_N	M	σ_M (10^{-2})
^{42}Ca	0° –25°	4	421	21	41.88	1.15
^{42}Ca	0° –25°	5	350	19	41.88	1.30
^{42}Ca	0° –25°	6	309	18	41.90	1.28
^{42}Ca	0° –25°	7	261	17	41.91	1.38
^{42}Ca	0° –25°	8	228	15	41.90	1.49
^{42}Ca	25° –50°	2	474	23	41.86	1.51
^{42}Ca	25° –50°	3	768	30	41.89	1.24
^{42}Ca	25° –50°	4	552	26	41.91	1.52
^{42}Ca	25° –50°	5	434	23	41.91	1.85
^{42}Ca	25° –50°	6	318	19	41.88	2.03
^{42}Ca	25° –50°	7	219	16	41.85	2.33
^{42}Ca	25° –50°	8	151	14	41.88	3.43
^{43}Ca	0° –25°	2	273	17	42.78	1.52
^{43}Ca	0° –25°	3	545	24	42.84	1.10
^{43}Ca	0° –25°	4	416	21	42.87	1.26
^{43}Ca	0° –25°	5	363	19	42.83	1.28
^{43}Ca	0° –25°	6	331	19	42.85	1.33
^{43}Ca	0° –25°	7	277	17	42.85	1.41
^{43}Ca	0° –25°	8	260	16	42.86	1.40
^{43}Ca	25° –50°	2	500	25	42.79	1.72
^{43}Ca	25° –50°	3	875	33	42.85	1.26
^{43}Ca	25° –50°	4	570	26	42.85	1.55
^{43}Ca	25° –50°	5	411	23	42.85	2.10
^{43}Ca	25° –50°	6	310	20	42.89	2.31
^{43}Ca	25° –50°	7	242	17	42.85	2.44
^{43}Ca	25° –50°	8	182	15	42.81	2.96
^{44}Ca	0° –25°	2	292	17	43.73	1.50
^{44}Ca	0° –25°	3	584	25	43.78	1.00
^{44}Ca	0° –25°	4	462	22	43.84	1.14
^{44}Ca	0° –25°	5	427	21	43.83	1.12
^{44}Ca	0° –25°	6	334	19	43.83	1.28
^{44}Ca	0° –25°	7	285	17	43.81	1.37
^{44}Ca	0° –25°	8	255	16	43.83	1.37
^{44}Ca	25° –50°	2	527	25	43.75	1.49
^{44}Ca	25° –50°	3	880	32	43.80	1.11
^{44}Ca	25° –50°	4	614	26	43.83	1.29
^{44}Ca	25° –50°	5	458	23	43.84	1.61
^{44}Ca	25° –50°	6	304	19	43.84	2.04
^{44}Ca	25° –50°	7	253	17	43.81	2.14
^{44}Ca	25° –50°	8	182	14	43.86	2.44

different isotopes. This correction on the ratios of interest varies from ∼3% for Range 2 ^{38}Ar/^{36}Ar to ∼12% for Range 2 ^{31}P/^{32}S and is discussed in more detail and tabulated in Ogliore (2007). As described earlier, nuclei that fragment in the CRIS detector stack are removed from the data set. The probability for a given nucleus to fragment depends on the mass of the nucleus, so it is necessary to correct for this when comparing CRIS abundances of different isotopes. The calculated survival probability for species of interest in this study varies from 89% for Range 2 ^{31}P to 56% for range 8 ^{44}Ca. At most, the fragmentation correction for the isotope ratios is ∼3%; details for this correction are also discussed in Ogliore (2007). A conservative error estimate of 3% is assigned to this correction.

The final corrected isotope ratios are also given in Tables 2–5. The 1σ uncertainty on the ratio is the quadrature sum of the uncertainty derived from the maximum likelihood fit (close to statistical uncertainty) and the systematic uncertainty from the fragmentation correction.

Table 2
Phosphorus Isotope Data

Range	Median Energy (MeV nucleon^{-1})	Number of Events ^{31}P	Final Corrected Ratio ^{31}P/^{32}S
2	117	739	0.209 ± 0.012
3	157	1544	0.256 ± 0.012
4	201	1208	0.242 ± 0.012
5	238	992	0.248 ± 0.014
6	270	808	0.252 ± 0.015
7	303	684	0.250 ± 0.016
8	332	709	0.278 ± 0.018

3. SOURCE ABUNDANCES

To calculate the isotope ratios of phosphorus, sulfur, argon, and calcium at the GCR source, the physical changes a GCR species undergoes during propagation through the interstellar medium must be taken into account. The quantity of a given isotope observed at Earth is the sum of a primary component that originated at the GCR source and a secondary component that is produced by spallation on interstellar atoms during cosmic ray propagation. Isotopes observed in the GCRs near Earth but absent from the source can be used to estimate the secondary production of the partially primary isotope of interest if they have similar spallation parentage. This is the "tracer method," described in Stone & Wiedenbeck (1979) and used to calculate the ^{22}Ne/^{20}Ne source ratio in Binns et al. (2005). The isotopes ^{33}S, ^{36}S, ^{42}Ca, and ^{43}Ca are much more abundant in the GCRs observed by CRIS than in the material ejected by supernovae (Rauscher et al. 2002) or seen in the solar system (Lodders 2003), so these isotopes are used to trace the secondary production of the partially primary isotopes of P, S, Ar, and Ca.

A steady-state leaky-box propagation model (Meneguzzi et al. 1971; Yanasak et al. 2001) is employed to derive GCR interstellar spectra. Particle fluxes are the result of a balance between acceleration, ionization energy loss, escape from the Galaxy, radioactive decay, and production and loss due to spallation. In this model, it is assumed that propagation follows acceleration and there is no reacceleration as the cosmic rays propagate through the Galaxy. The leaky-box transport equation is

$$0 = q_i f_i(\epsilon) - \frac{\varphi_i}{\Lambda_i} + \sum_{j \neq i} \frac{\varphi_j}{\Lambda_{ji}} + \frac{\partial}{\partial \epsilon}(w_i \varphi_i), \quad (1)$$

where q_i is the source abundance of species i with source spectral shape $f_i(\epsilon)$, ϵ is the energy per nucleon, and w_i is the specific ionization per nucleon of species i. The terms on the right-hand side of Equation (1) represent the production of i by the source, the destruction of i by fragmentation or radioactive decay during propagation through the Galaxy, the production of i from the fragmentation or radioactive decay of heavier nuclei j during propagation, and changes in the spectral shape due to ionization energy loss. The cosmic rays that come from the source $q_i f_i(\epsilon)$ are primary cosmic rays; those produced by the fragmentation of heavier nuclei are secondary cosmic rays. Equation (1) contains the mean free paths for production (Λ_{ji}) and for loss (Λ_i), which themselves represent several distinct processes:

$$\frac{1}{\Lambda_{ji}} = \frac{\sigma_{ji}^{H} + (n_{\rm He}/n_{\rm H})\sigma_{ji}^{\rm He}}{M_H + (n_{\rm He}/n_{\rm H})M_{\rm He}} + \frac{1}{\rho v \tau_{ji} \gamma} \quad (2)$$

$$\frac{1}{\Lambda_i} = \frac{1}{\Lambda_i^{\rm esc}} + \frac{\sigma_i^{H} + (n_{\rm He}/n_{\rm H})\sigma_i^{\rm He}}{M_H + (n_{\rm He}/n_{\rm H})M_{\rm He}} + \frac{1}{\rho v \tau_i \gamma}. \quad (3)$$

The escape-probability from the Galaxy in the leaky-box model is manifested in Equation (3) as $\Lambda_i^{\rm esc}$, the escape mean free path for i. The total destruction cross sections for the nucleus i by collision with interstellar hydrogen and helium are σ_i^H and $\sigma_i^{\rm He}$, respectively, $n_{\rm H}$ and $n_{\rm He}$ are the number densities of hydrogen and helium in the interstellar medium, $M_{\rm H}$ and $M_{\rm He}$ are the masses of hydrogen and helium atoms, σ_{ji}^H and $\sigma_{ji}^{\rm He}$ are the cross sections for the production of the nucleus i from the spallation of nucleus j by hydrogen and helium respectively, and the mass density of the interstellar medium is $\rho = n_{\rm H} M_H + n_{\rm He} M_{\rm He}$. The decay of radioactive isotopes with lifetimes comparable to the 15 million year mean residence time of cosmic rays in the Galaxy is accounted for by the last term in the above equations, with v representing the particle's velocity, γ the corresponding Lorentz factor, τ_i the mean lifetime for the decay of i, and τ_{ji} the mean lifetime for the decay of isotope j to isotope i.

The HEAO-3-C2 instrument measured cosmic rays at energies from 0.6 to 35 GeV nucleon^{-1}, where solar modulation does not greatly alter the spectral shape of the nuclei over most of the energy interval. Leaky-box calculations by Engelmann et al. (1990) showed that source spectra proportional to a power law in momentum per nucleon, P, fit these measurements well. For this work, we assume the source spectral shape to be

$$f_i(\epsilon) \propto P^{-2.35}. \quad (4)$$

Previously calculated cosmic ray source abundances, where available, were used for q_i in Equation (1) (as in Wiedenbeck et al. 2001b), and solar system composition with fractionation effects was assumed for those nuclides i where nominal cosmic ray abundances are not known.

Energy-dependent cross-section measurements are needed to calculate the spallation of a nucleus to a lighter species due to collisions with particles in the ISM (assumed to be 90% hydrogen and 10% helium by number). The semiempirical cross-section formulae of Webber et al. (1990) are used. A large data set of direct cross-section measurements was compiled and used to scale the Webber formulae to experimental measurements for the reactions where this data is available (see Ogliore 2007 for more details). One of the most important parent nuclei for the production of P, S, Ar, and Ca during propagation is ^{56}Fe because of its high abundance in the GCRs and moderate cross section for producing isotopes in the mass range of 30–50. Spallation of ^{56}Fe produces between ~10% and ~40% of the total secondary contribution of GCR P, S, Ar, and Ca nuclei arriving at Earth. Measurements of the spallation products of ^{56}Fe nuclei accelerated into a liquid hydrogen target (Villagrasa-Canton et al. 2007) over the energy range 300–1500 MeV nucleon^{-1} provided experimental data to better estimate this important contribution to the GCR secondary component.

The interstellar energy spectra of all the parent nuclei for the isotope of interest are calculated, then the spectra at Earth are calculated using a spherically symmetric solar modulation model for transport from the interstellar medium to the inner heliosphere (Fisk 1971). These modulated spectra may differ from the CRIS observations due to uncertainties in the spallation cross sections or incorrect source abundances. It is assumed that an overall scale factor will bring the modeled spectra into agreement with the observations, so the interstellar parent spectra are scaled to match the observations as shown in Figure 4. This effectively removes the necessity to know spallation cross sections for all reactions except those that generate the isotopes of interest (Wiedenbeck et al. 2007a, 2007b). For example, to calculate the source abundance of ^{34}S, it

Table 3
Sulfur Isotope Data

Range	Median Energy	Number of Events				Final Corrected Ratio		
	(MeV nucleon^{-1})	^{32}S	^{33}S	^{34}S	^{36}S	^{33}S/^{32}S	^{34}S/^{32}S	^{36}S/^{32}S
2	122	3948	587	770	38	0.153 ± 0.010	0.205 ± 0.012	0.0106 ± 0.0019
3	165	6619	1122	1409	63	0.174 ± 0.009	0.224 ± 0.011	0.0106 ± 0.0015
4	211	5400	915	1065	67	0.173 ± 0.010	0.208 ± 0.011	0.0139 ± 0.0020
5	250	4276	846	1003	71	0.202 ± 0.012	0.247 ± 0.014	0.0185 ± 0.0027
6	285	3396	713	827	44	0.214 ± 0.013	0.256 ± 0.015	0.0143 ± 0.0027
7	318	2884	645	739	28	0.228 ± 0.015	0.270 ± 0.017	0.0109 ± 0.0026
8	349	2669	565	717	40	0.216 ± 0.015	0.283 ± 0.018	0.0169 ± 0.0035

Table 4
Argon Isotope Data

Range	Median Energy	Number of Events				Final Corrected Ratio		
	(MeV nucleon^{-1})	^{36}Ar	^{37}Ar	^{38}Ar	^{40}Ar	^{37}Ar/^{36}Ar	^{38}Ar/^{36}Ar	^{40}Ar/^{36}Ar
2	130	890	427	749	103	0.493 ± 0.037	0.895 ± 0.059	0.1315 ± 0.0158
3	176	1452	762	1600	176	0.538 ± 0.034	1.161 ± 0.064	0.1352 ± 0.0131
4	224	1191	664	1159	144	0.570 ± 0.039	1.017 ± 0.061	0.1324 ± 0.0143
5	267	997	540	1073	131	0.552 ± 0.041	1.118 ± 0.072	0.1420 ± 0.0165
6	305	781	491	885	107	0.641 ± 0.052	1.173 ± 0.083	0.1460 ± 0.0192
7	341	713	422	677	91	0.602 ± 0.053	0.979 ± 0.076	0.1349 ± 0.0198
8	373	631	368	719	74	0.592 ± 0.056	1.172 ± 0.094	0.1234 ± 0.0202

Table 5
Calcium Isotope Data

Range	Median Energy	Number of Events					Final Corrected Ratio			
	(MeV nucleon^{-1})	^{40}Ca	^{41}Ca	^{42}Ca	^{43}Ca	^{44}Ca	^{41}Ca/^{40}Ca	^{42}Ca/^{40}Ca	^{43}Ca/^{40}Ca	^{44}Ca/^{40}Ca
2	137	1938	409	863	923	979	0.216 ± 0.016	0.468 ± 0.028	0.512 ± 0.031	0.560 ± 0.033
3	185	3421	750	1601	1780	1841	0.224 ± 0.014	0.488 ± 0.025	0.555 ± 0.028	0.587 ± 0.029
4	236	2581	602	1297	1318	1445	0.238 ± 0.016	0.521 ± 0.029	0.541 ± 0.030	0.601 ± 0.032
5	281	2000	532	1118	1106	1266	0.270 ± 0.020	0.576 ± 0.034	0.583 ± 0.035	0.673 ± 0.039
6	323	1613	441	951	976	974	0.278 ± 0.022	0.606 ± 0.039	0.635 ± 0.041	0.637 ± 0.040
7	360	1365	369	775	842	876	0.274 ± 0.024	0.581 ± 0.040	0.646 ± 0.044	0.673 ± 0.045
8	396	1154	352	651	765	760	0.309 ± 0.029	0.576 ± 0.044	0.692 ± 0.051	0.686 ± 0.050

is not necessary to know the cross section to produce ^{40}Ca from ^{44}Ti since the ^{40}Ca spectrum is scaled to CRIS observations.

The free parameters of the tracer leaky-box calculation are the source abundances of the two isotopes of interest and the escape mean free path, $\Lambda^{\rm esc}$, which is assumed to take the form given in Davis et al. (2000):

$$\Lambda^{\rm esc} = \frac{\Lambda_0 \beta}{\left(\frac{\beta R}{1.0\ {\rm GV}}\right)^{0.6} + \left(\frac{\beta R}{1.3\ {\rm GV}}\right)^{-2.0}}, \quad (5)$$

where β is the particle's velocity divided by the speed of light, R is the particle's rigidity, and Λ_0 is an overall normalization factor. A larger $\Lambda^{\rm esc}$ means the cosmic rays have traversed more material and thus more primary particles have fragmented into lighter secondaries. In this manner, the measured spectra of the tracer isotopes determine $\Lambda^{\rm esc}$, and consequently, the secondary component of the partially primary isotopes. The determination of source abundances can be thought of as a minimization problem, where the quantity to be minimized is a χ^2 between the leaky-box-modeled, solar-modulated spectra and the CRIS observations, with the uncertainties being a quadrature sum of uncertainties in the modeled spectra and statistical uncertainties in the CRIS measurements. The solar modulation parameter was calculated to be 494 ± 34 MV from a separate implementation of the leaky-box calculation. This value is in agreement with the modulation parameter as calculated from CRIS spectral shapes (Wiedenbeck et al. 2005).

The leaky-box model spectra are uncertain due to the spallation cross sections. An uncertainty is associated with each spallation cross-section reaction. The Webber formulae are assumed to be 25% uncertain; Webber et al. (1990) claim 10% uncertainties, but analysis of other semiempirical formulae after more data became available yields uncertainties up to 35% (Raisbeck 1979). If cross-section data exists to scale the Webber formulae, the uncertainty is recalculated taking into account the quoted errors on the measurements. The data-normalized cross sections have uncertainties ranging from 5% to 15%.

The source abundances are determined by finding the minimum χ^2 of the pair of isotopes of interest and the four tracers simultaneously. The source abundances of the partially primary isotopes are varied along with the overall normalization of the escape mean free path (Λ_0 in Equation (5)) until the solar-modulated leaky-box spectra match the CRIS observations. The leaky-box spectra and CRIS observations are shown for the four tracers and seven partially primary isotopes in Figure 5; the

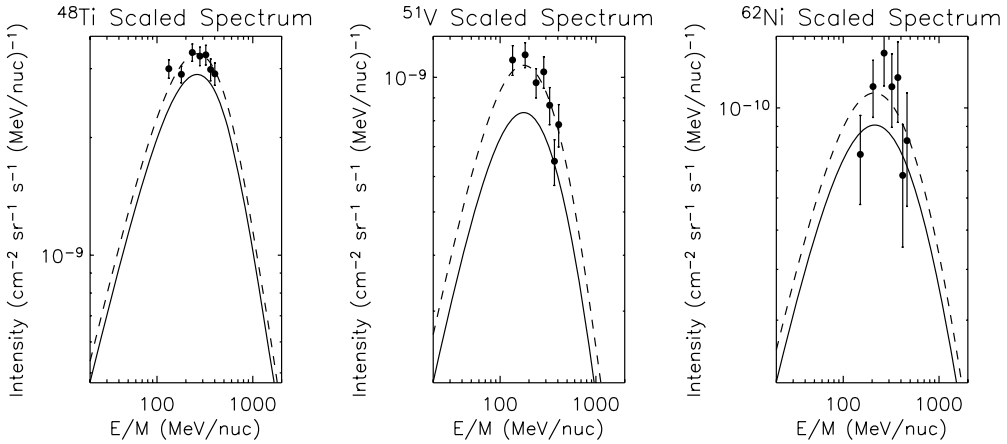

Figure 4. Modulated model spectra (solid lines) are multiplied by a constant to fit CRIS measurements (circles) to obtain scaled spectra at Earth (dashed lines). Shown here are three examples of scaled spectra. The predicted spectral shape of the models is reasonably close to the observations, so only the overall magnitude needs to be adjusted to fit the data.

secondary contributions to the isotope spectra are given by the dashed lines (equal to the total spectra for the tracer isotopes). Measurement uncertainties are indicated by the error bars on the points; model (cross section) uncertainties are indicated by the dotted lines.

Uncertainties of the source abundances can also be calculated based on the cross-section uncertainties and CRIS measurement errors. The source abundance of each isotope will have an optimal value at the minimum χ^2, and the 1σ uncertainty will be at minimum $\chi^2 + 1$ (Orear 1982). Correlated uncertainties exist between the source abundance and the escape mean free path $\Lambda^{\rm esc}$, so 1σ error ellipses are computed to determine the maximal correlated error between these two parameters. The source abundance uncertainty correlations with the uncertainty in the modulation parameter, ± 34 MV, was found to be insignificant, giving these results robustness over a range of values for the solar modulation parameter near solar minimum. The minimization problem has 39 degrees of freedom (dof): 42 measured intensities (two partially primary isotopes and four tracer isotopes, with seven intensities for each isotope corresponding to the ranges of CRIS events) minus three free parameters to be fit (the abundances of the two partially primary isotopes, and the escape mean free path). The optimal reduced χ^2 values for the source abundance calculations were between 1.0 and 1.2.

The GCR source abundance ratios for the isotopes of P, S, Ar, and Ca are given in Table 6, along with the solar system ratio from Lodders (2003). Also listed in Table 6 are the ratios calculated in two GALPROP models for comparison (Moskalenko et al. 2007). The GALPROP code solves a set of transport equations for all cosmic ray species and has a detailed treatment of the physics involved in cosmic ray propagation throughout the Galaxy (Strong et al. 2007). The propagated abundances were adjusted to CRIS observations using an iterative procedure. Although the GALPROP model employs a completely different technique, the source ratios obtained in the two models (diffusive reacceleration and plain diffusion) are close to the ratios derived in this work, indicating that the results are very robust. The source of the notable deviations in the case of Ar isotopes is not known with certainty and will be investigated in future work.

For a number of the nuclides considered in this study, the abundances in the cosmic rays arriving at Earth contain sizeable contributions from secondary material produced during propagation, as shown in Figure 5. Relatively small fractional uncertainties in the corrections that must be made for these secondary contributions can lead to larger fractional uncertainties in the derived source abundances. In this region of the periodic table, the production of secondaries is due to the fragmentation of a sizeable number of heavier nuclides that make comparable contributions. The total uncertainty on the secondary production of the P, S, Ar, and Ca isotopes during GCR propagation due to (assumed uncorrelated) cross-section uncertainties for all the spallation parent nuclei is calculated to be between 2.9% and 4.8%. These uncertainties are shown as dotted lines in the modeled spectra in Figure 5.

The tracer isotopes can be used to check this total cross-section uncertainty. From Equation (1), ignoring energy loss, which will not change interstellar abundances, we see for a tracer isotope with no source abundance:

$$\varphi_i = \Lambda_i \sum_{j \neq i} \frac{\varphi_j}{\Lambda_{ji}}. \quad (6)$$

The loss mean free path Λ_i is determined by the purely secondary tracer isotopes of ^{33}S, ^{36}S, ^{42}Ca, and ^{43}Ca. Since the loss balances the production in the steady-state leaky-box model, the uncertainty in the derived mean Λ_i for the ensemble of tracers reflects the variation of the production of individual tracers. Since the production variation of an individual tracer should just be the total cross-section uncertainty for that tracer (2.9%–4.8%), we can use the variance in Λ_i given by the ensemble of tracers to see if our total cross-section uncertainty estimates are reasonable.

For each tracer isotope, the loss mean free path Λ_i and its uncertainty are calculated by the χ^2-minimization procedure described previously. The uncertainty on the mean of these four values is $\sim$1.7%. The average variance of the ensemble is the square root of the number of tracers times $\sim$1.7%, which is $\sim$3.4%. Since $\sim$3.4% is consistent with the range of total cross-section uncertainties, 2.9%–4.8%, we conclude that these cross-section uncertainties are reasonable. The partially primary isotopes have similar parents as the tracers, so the uncertainty on the production of these isotopes is about the same as the tracer production uncertainty (assuming that the measured cross-section data is available for the tracer isotope as it is for the partially primary isotopes, which is the case for

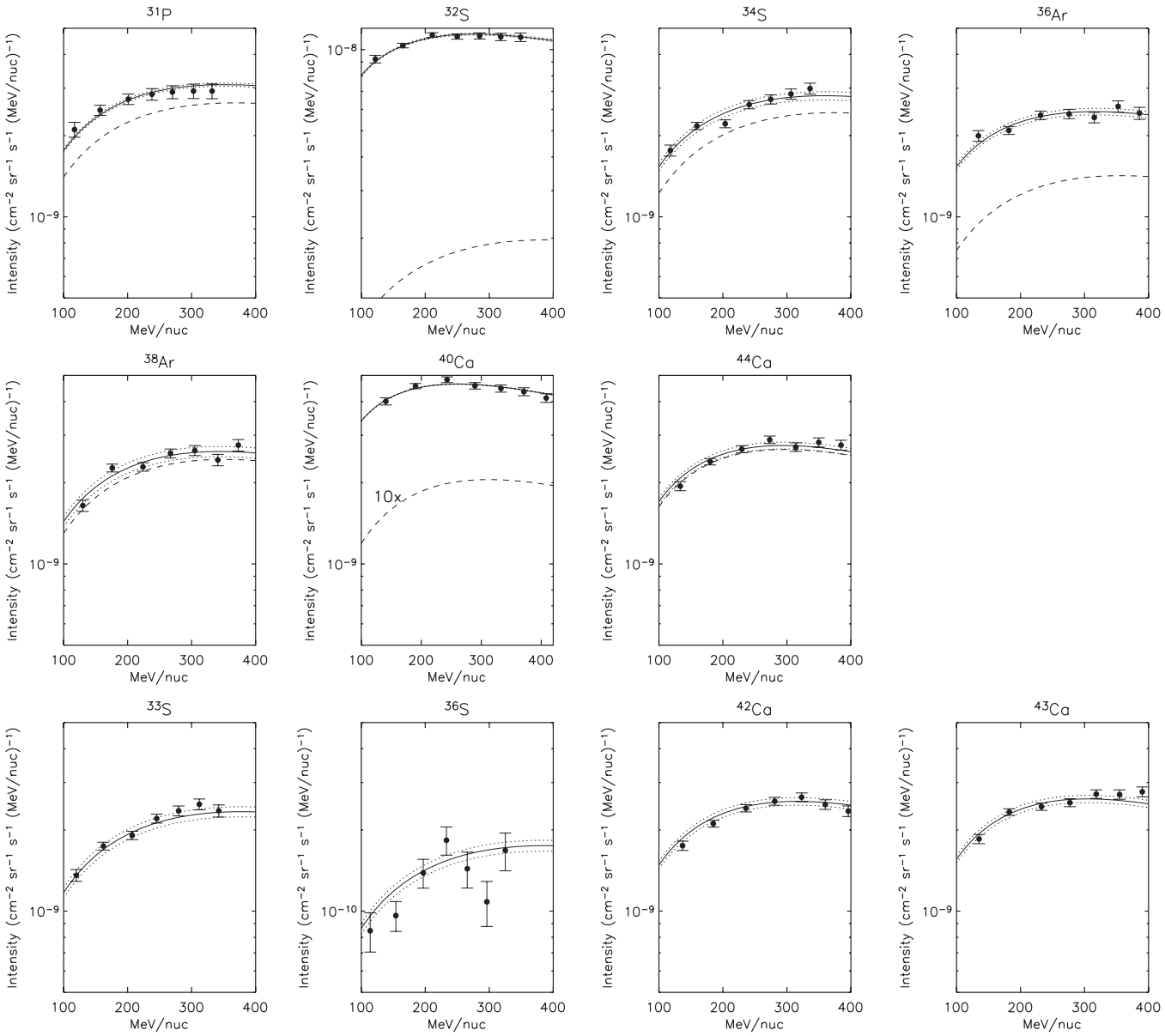

Figure 5. CRIS solar minimum observations (circles, with 1σ statistical uncertainties) are plotted with the model spectra (solid lines) for the optimal source abundances of ^{31}P, ^{32}S, ^{34}S, ^{36}Ar, ^{38}Ar, ^{40}Ca, and ^{44}Ca, and optimal escape mean free path coefficient ($\Lambda_0 = 20.3 \pm 0.8$ g cm^{-2}). The dashed lines show the secondary contribution to these isotopes. The tracer isotopes (plotted on the bottom row) ^{33}S, ^{42}Ca, ^{43}Ca, and ^{36}S have no source abundance. The dotted lines are the model errors due to uncertainty in the secondary production from cross-section uncertainties.

this set of isotopes). The total production uncertainty is significantly smaller than the individual cross-section uncertainties from a single reaction because many cross sections go into the production of an isotope from all of its spallation parents. As mentioned earlier, cross-section uncertainties are assumed to be uncorrelated, so the uncertainty on the total production of a given isotope can be quite small as cross-section errors average out, yielding the rather modest source abundance uncertainties given in Table 6. The assumption of uncorrelated cross-section errors cannot be strictly valid; some correlations can be expected due to systematic errors that affect multiple cross sections measured in the same experiment as well as to the use of semiempirical formulae to estimate cross sections that have not been measured. Hinshaw & Wiedenbeck (1983) compared the uncertainties in derived elemental source abundances for the cases of fully uncorrelated and fully correlated cross-section errors. As an example, they found that if all partial cross sections have 35% uncertainties, then these result in an uncertainty in the source abundance of P of 25% with no correlations and ∼70% with full correlation. Since the time of that study many of the most important cross sections have been measured, resulting in smaller uncertainties and less correlation. An investigation of the extent to which correlations of cross-section errors could realistically affect the accuracy of the source abundances that we have presented is beyond the scope of the present study but the possibility of correlations should be kept in mind when using our results.

Thayer (1997) measured the ^{34}S/^{32}S ratio in the heliosphere to be 0.242 ± 0.027 over an energy range approximately equivalent to CRIS ranges 2–5. This value is consistent with the CRIS ^{34}S/^{32}S ratios, given in Table 3. Thayer then estimated the ^{34}S/^{32}S GCR source ratio to be $0.062 \pm 0.026 \leqslant 0.029$, where the first error is statistical and the second is due to uncertainty in the propagation calculation. This value is more uncertain, but

Table 6
Derived Isotope Ratios at the GCR Source

Ratio	GCR Source[a]	GALPROP DR[b]	GALPROP PD[c]	Solar System[d]
$^{31}P/^{32}S$	0.046 ± 0.006	0.047	0.047	0.0198
$^{34}S/^{32}S$	0.039 ± 0.005	0.038	0.035	0.0444
$^{38}Ar/^{36}Ar$	0.16 ± 0.04	0.065	0.049	0.1818
$^{44}Ca/^{40}Ca$	0.020 ± 0.011	$\sim$0	$\sim$0	0.0215
$^{36}Ar/^{40}Ca$	0.224 ± 0.009	0.19	0.18	1.423

Notes.
[a] This work.
[b] GALPROP Diffusion Reacceleration Model (Moskalenko et al. 2007).
[c] GALPROP Plain Diffusion Model (Moskalenko et al. 2007).
[d] As given by Lodders (2003).

consistent with, the value derived here (0.039 ± 0.005, Table 6). George et al. (2001) calculated the source $^{31}P/^{32}S$ ratio using CRIS data and a variation of the tracer technique employed here and found the value to be 0.065 ± 0.01, within 2σ of the value derived in this work.

4. DISCUSSION

4.1. Superbubble Composition

The acceleration site and compositional source of GCRs is likely the cores of superbubbles. Superbubbles contain a mixture of interstellar medium material and ejecta from core-collapse supernovae and massive star winds. The superbubble material from which GCRs are accelerated is assumed to be composed of 80% ISM and 20% ejecta, based on the analysis of the $^{22}Ne/^{20}Ne$ GCR source ratio and other isotope ratios (Higdon & Lingenfelter 2003; Binns et al. 2005), as well as the elements Si, C, O, and Fe (Lingenfelter & Higdon 2007). The composition of the superbubble interior or, equivalently, the GCR seed material, is calculated here based on Higdon & Lingenfelter (2003) and Lingenfelter & Higdon (2007).

The superbubble-progenitor OB association is assumed to have a Salpeter initial mass function (IMF; $dN/dM \propto M^{-2.35}$; Salpeter 1955), consistent with the observations of nearby OB associations (Massey et al. 1995). A star with mass greater than 8 $M_\odot$ and less than 25 $M_\odot$ will explode as a Type II supernova. For initial masses greater than 25–40 $M_\odot$ (depending upon the star's metallicity and whether the rotation is taken into account) the star will enter the W–R phase (Meynet & Maeder 2005), lose its outer envelope to winds, and explode as a Type Ib/c supernova if the stellar metallicity is roughly solar or less (Heger et al. 2003). Stars with very large initial masses and metallicity somewhat less than solar will collapse into a black hole and accrete the material that is expelled in the supernova. No material is injected into the environment, so nothing is contributed to the cosmic-ray seed population. The lower limit mass for black hole formation is taken to be 40 $M_\odot$ (Fryer 1999). A fraction of Type Ia supernovae (explosions of white dwarf stars which live much longer than a superbubble) occur inside the superbubble by chance, and will contribute their ejecta to the GCR seed material in the superbubble core.

The accumulated freshly synthesized ejecta material inside the superbubble comes from core-collapse supernovae of Type II and Type Ib/c, W–R winds, and Type Ia supernovae. The SNII ejecta yields used in this work are from Woosley & Weaver (1995) from 8 $M_\odot$ to 15 $M_\odot$ and Rauscher et al. (2002) from 15 $M_\odot$ to 25 $M_\odot$. For SNIbc, yields as a function of the progenitor star's helium core mass as calculated by Woosley et al. (1995) are used. Results from Arnett (1978) were used to relate the helium core mass to the star's initial main-sequence mass. The massive-star models of Meynet et al. (2001) were used by S. Goriely (2005, private communication) to calculate abundances in the W–R winds ejected between the star's birth and the end of the W–R phase for initial stellar masses 40 $M_\odot$, 60 $M_\odot$, and 85 $M_\odot$ (see also Binns et al. 2005; Arnould et al. 2006). Type Ia supernovae were assumed to occur at a rate of 0.3 per century uniformly in the galaxy (van den Bergh & McClure 1994; Hatano et al. 1997). The "W7 model" yields of Iwamoto et al. (1999) were used to calculate the SN Ia contributions to the superbubble core, taken to be within the inner 30% of the superbubble radius (Westphal & Bradley 2004). The ejected masses of ^{32}S and ^{34}S per star from SNII, SNIbc, and W–R stars, weighted by the Salpeter IMF are shown in Figure 6.

The GCRs observed at Earth are likely to be a sample of matter from a number of superbubbles, instead of just from a single OB association. There are $\sim$20 OB associations within 500 pc of the solar neighborhood (Binns et al. 2007), the region where most GCRs of a few hundred MeV nucleon^{-1} are likely to originate (Streitmatter et al. 1985). This ensemble is a sample of superbubbles in various stages of their evolution, so to calculate the composition of the GCR seed material, it is necessary to derive the time evolution of the superbubble composition and then take a time average over the cosmic-ray-accelerating lifetime of the superbubble. Since GCRs are likely to be only accelerated when supernova shocks are present in the superbubble, this average should be weighted by the supernova rate. The stellar initial mass–lifetime relationship derived by Higdon & Lingenfelter (2003) from data in Schaller et al. (1992) for 7–120 $M_\odot$ is given by

$$\ln t_\star(M) = C_5 + C_4 \ln M + C_3(\ln M)^2 + C_2(\ln M)^3 + C_1(\ln M)^4, \quad (7)$$

where $C_{1-5} = [0.0119914, -0.218395, 1.69502, -6.6851, 11.9115]$; t is in Myr and M has units of solar masses. The relative supernova rate in the superbubble, dN/dt, can be deduced simply from Equation (7) and the Salpeter IMF, $dN/dt = (dN/dM)(dM/dt)$. The accumulated ejecta mass of an isotope in a superbubble as a function of time is calculated by integrating the yields weighted by the frequency of events producing the ejecta, dN/dt, over the lifetime of supernovae activity in the superbubble from $\sim$3 to $\sim$37 Myr after star formation (the association is assumed to be coeval), corresponding to the lifetime of a 25 $M_\odot$ star and an 8 $M_\odot$ star, respectively. Seemingly all supernovae, independent of the progenitor star's mass, release about 10^{51} erg of ejecta kinetic energy (see, e.g., Woosley & Weaver 1995), so we can assume that every supernova in the superbubble accelerates cosmic rays with approximately the same efficiency. The accumulated mass of ^{32}S and ^{34}S inside a superbubble of 150 stars is shown in Figure 7.

The time-averaged accumulated ejecta mass of an isotope, weighted by GCR-accelerating supernovae events, in a superbubble enclosing a coeval OB association is calculated by integrating the accumulated mass multiplied by dN/dt over the time period of supernovae activity. Dividing this quantity by the total accumulated mass of the ejecta of all elements yields the ejecta mass fraction of an isotope x, $(F_x)_{\rm ejecta}$. The abundance of isotope x in the superbubble will consist of a fraction $f_{\rm ej}$ of ejecta material and $1 - f_{\rm ej}$ ISM material. The interstellar isotopic mass fraction $(F_x)_{\rm ISM}$ is assumed to be the same as solar (Lodders 2003; unless astronomical observations of interstellar isotopic composition are available). The superbubble mass

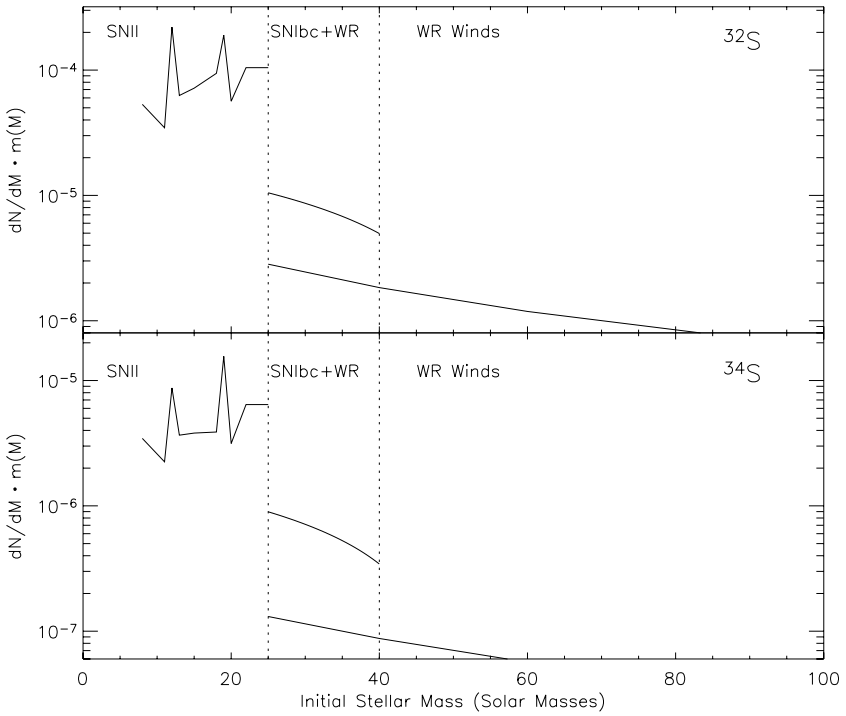

Figure 6. Ejected mass of ^{32}S and ^{34}S per star, weighted by the Salpeter IMF as a function of the star's initial mass. Type II supernovae contribute ejecta below 25 $M_{\odot}$, SNIb/c contribute ejecta between 25 $M_{\odot}$ and 40 $M_{\odot}$, and stars heavier than 25 $M_{\odot}$ eject material into the superbubble in the form of W–R winds.

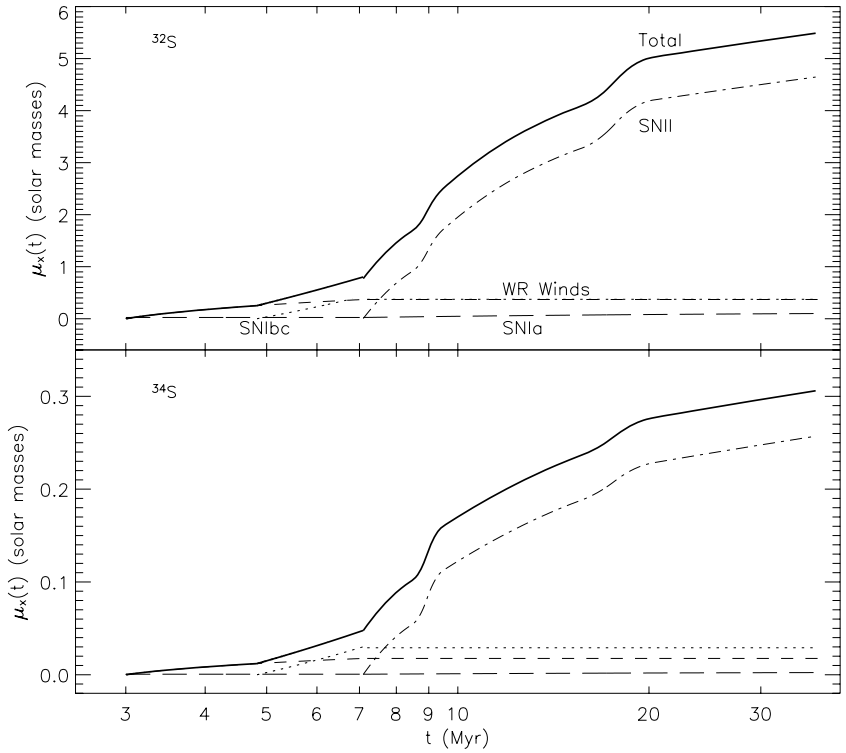

Figure 7. Accumulated ejecta mass, μ, of ^{32}S and ^{34}S in units of solar masses as a function of the superbubble age for a superbubble of 150 stars with Salpeter IMF. The accumulated ^{32}S and ^{34}S ejecta, as well as the ^{36}Ar, ^{38}Ar, ^{40}Ca, and ^{44}Ca ejecta, are dominated by Type II (dot-dashed line) supernova ejecta for the majority of the superbubble lifetime. W–R winds (short-dashed line), Type Ibc supernovae (dotted line), and Type Ia supernovae (long-dashed line) do not contribute much to the total accumulated ejecta mass of these isotopes.

fraction of x is

$$(F_x)_{\rm sb} = (1 - f_{\rm ej})(F_x)_{\rm ISM} + f_{\rm ej}\,(F_x)_{\rm ejecta}\,. \quad (8)$$

The superbubble isotope number ratios, which are needed to compare with the GCR observations, are the ratios of these mass fractions multiplied by the inverse of the isotope masses, e.g.,

$$\left(\frac{^{34}{\rm S}}{^{32}{\rm S}}\right)_{\rm sb} = \frac{32}{34}\frac{\left(F_{^{34}{\rm S}}\right)_{\rm sb}}{\left(F_{^{32}{\rm S}}\right)_{\rm sb}}. \quad (9)$$

4.2. FIP and Volatility

The derived ^{31}P/^{32}S GCR source ratio of 4.63% ± 0.64% is a factor of 2.34 ± 0.34 larger than the solar system value. This enhancement could be a result of preferential acceleration of the moderately volatile P over the volatile S, or it could be due to a larger amount of P in the GCR source environment. It is necessary, therefore, to calculate the ^{31}P/^{32}S ratio in the cosmic ray seed population to determine what is responsible for the ^{31}P/^{32}S enhancement in the GCRs observed at Earth.

The ^{31}P/^{32}S superbubble ratio, calculated as described above with $f_{\rm ej} = 0.2$ (derived from other GCR species as described earlier) is equal to 2.46%, or ∼1.24 times the solar system ratio. Therefore, the enhancement in the derived ^{31}P/^{32}S GCR source ratio is most likely due to a bias in the acceleration mechanism and not due to an isotopically anomalous source environment. Sulfur and phosphorus break the FIP–volatility correlation as mentioned earlier, so this enhancement in ^{31}P over ^{32}S lends support to the suggestion that volatility is the controlling parameter in the observed fractionation of the GCRs. A number of previous studies (George et al. 2001; Ellison et al. 1997) have used various elemental abundance ratios to address the question of whether FIP or volatility is the parameter controlling the observed fractionation. Most have favored volatility, but without sufficient statistical significance to be regarded as conclusive.

4.3. Dust/Grain Composition of ISM and Supernova Ejecta

The acceleration efficiency of dust-forming GCR species compared to gas-phase species can be investigated within the set of GCR source abundances derived in this work. Argon, a noble gas, will exist solely in the gas phase inside the superbubble. Conversely, calcium is almost completely depleted out of the gas phase in the interstellar medium and must be confined in dust grains (Savage & Sembach 1996; Jenkins 2004), so it mostly exists in grains in the GCR seed material. Therefore, the ^{36}Ar/^{40}Ca ratio in the GCR source relative to the solar system provides a way to measure the efficiency for accelerating grains compared to that for accelerating gas over this mass and charge range.

In the superbubble core the expected ^{36}Ar/^{40}Ca ratio is calculated as was done earlier for ^{31}P/^{32}S and was found to be 1.46, which is close to the solar system ratio of 1.42. The GCR source ^{36}Ar/^{40}Ca ratio is 0.224 ± 0.009, which is a factor of 6.4 ± 0.3 smaller than the solar system ratio. Therefore, the lower value in the GCR source ratio can be attributed to the increased acceleration efficiency for dust grains. This provides the grain/gas efficiency factor that will be used in the following calculations.

Assuming that the ISM and ejecta material inside the superbubble can be either in grain or gas form, Equation (8) becomes

$$\begin{aligned}(F_x)_{\rm sb} = {} & \left(d^x_{\rm ISM}\right)(\varepsilon_{\rm dust})(1 - f_{\rm ej})(F_x)_{\rm ISM} \\ & + \left(1 - d^x_{\rm ISM}\right)(1 - f_{\rm ej})(F_x)_{\rm ISM} \\ & + \left(d^x_{\rm ejecta}\right)(\varepsilon_{\rm dust})f_{\rm ej}(F_x)_{\rm ejecta} \\ & + \left(1 - d^x_{\rm ejecta}\right)f_{\rm ej}(F_x)_{\rm ejecta}, \end{aligned} \quad (10)$$

where $\varepsilon_{\rm dust}$ is 6.4, $f_{\rm ej}$ is 0.2, $d^x_{\rm ISM}$ is the dust fraction of isotope x in the ISM, and $d^x_{\rm ejecta}$ is the dust fraction of isotope x in the ejecta.

4.3.1. $^{34}S/^{32}S$ at the GCR Source

The mass fraction of the sulfur isotopes ^{32}S and ^{34}S at the GCR source can be calculated from Equation (10). The interstellar mass fraction of the sulfur isotopes, $(F_{^{32}{\rm S}})_{\rm ISM}$ and $(F_{^{34}{\rm S}})_{\rm ISM}$, is taken to differ from the solar system values based on a spectroscopic line survey of monosulfides in 20 star-forming regions by Chin et al. (1996). The ^{34}S/^{32}S ratio deduced near the Sun is ∼0.03, about 30% lower than the solar system ratio, taken to be the terrestrial ratio of 0.0444 given by Lodders (2003). The ejecta mass fractions, $(F_{^{32}{\rm S}})_{\rm ejecta}$ and $(F_{^{34}{\rm S}})_{\rm ejecta}$, are calculated as described in Section 4.1. ^{34}S is more abundantly synthesized relative to ^{32}S in the OB-association ejecta, resulting in an ejecta ^{34}S/^{32}S ratio of 0.053. A recent study of dust condensation in SN 1987A by Ercolano et al. (2007) shows a much lower dust condensation efficiency of refractories than previously estimated. Ercolano et al. (2007) suggest that a 20 $M_\odot$ star exploding as a supernova would condense only 0.05% of its refractory ejecta into grains. Therefore, it can be assumed that the amount of ejecta dust condensation of sulfur, a volatile, would be essentially zero. The ejecta dust fraction of the sulfur isotopes, $d^{^{32}{\rm S}}_{\rm ejecta}$ and $d^{^{34}{\rm S}}_{\rm ejecta}$, is taken to be zero. Interstellar sulfur is thought to exist solely in the gas phase in the diffuse interstellar medium (Savage & Sembach 1996; Snow & Witt 1996; Howk et al. 2006), but it has been historically assumed to be almost entirely depleted out of the gas phase onto dust grains in molecular clouds (Jansen et al. 1994; Tieftrunk et al. 1994; Millar & Herbst 1990). However, arguments have been made against large sulfur depletions in molecular clouds due to the absence of strong IR features due to sulfur-bearing ices, in addition to other issues as described in Goicoechea et al. (2006, and references therein). The fraction of sulfur in grains in the Horsehead photodissociation region was recently calculated to be less than 75% (Goicoechea et al. 2006), and can be very close to undepleted (100% gas phase) if the gas is warmer than 30 K. Grain-phase sulfur exists in interstellar dust grains called GEMS (Bradley et al. 1999), which have been proposed to be representative of the GCR source material (Westphal & Bradley 2004). The sulfur grain/gas fraction in different galactic environments is an interesting open question, one that observations of GCRs can possibly address. The calculated superbubble GCR ratio is plotted as a function of the fraction of interstellar sulfur in grains in Figure 8.

The derived GCR source ^{34}S/^{32}S ratio does not stringently constrain the ISM sulfur grain fraction within 1σ errors. The same analysis can be applied to the ^{31}P/^{32}S superbubble ratio, as shown in Figure 9. The ejecta grain fraction of moderately volatile phosphorus is assumed, like sulfur, to be zero. The fraction of interstellar phosphorus in grains was measured to

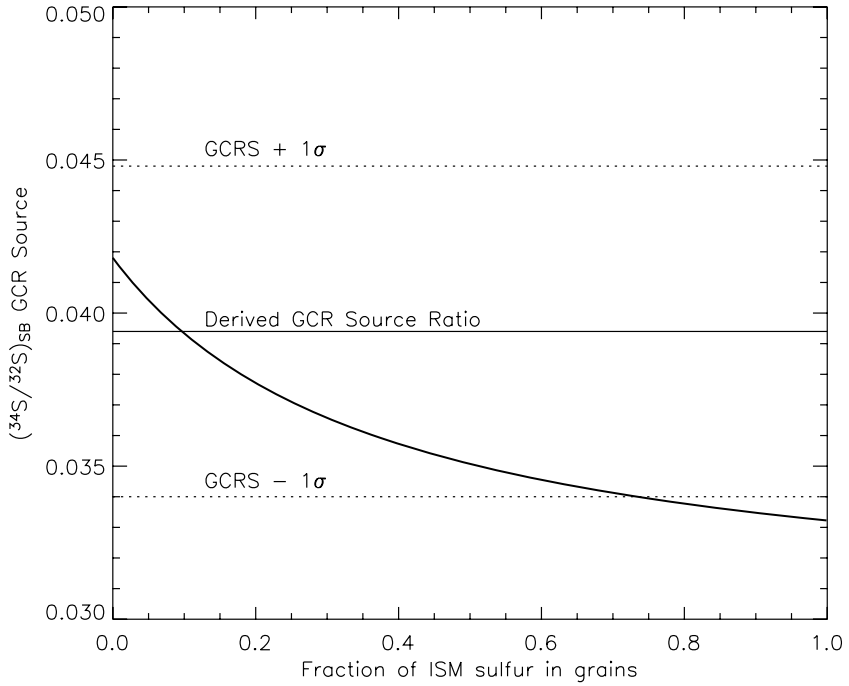

Figure 8. Superbubble $^{34}S/^{32}S$ ratio is plotted as a function of the fraction of interstellar sulfur in grains assuming that all of the sulfur ejecta is in the gas phase.

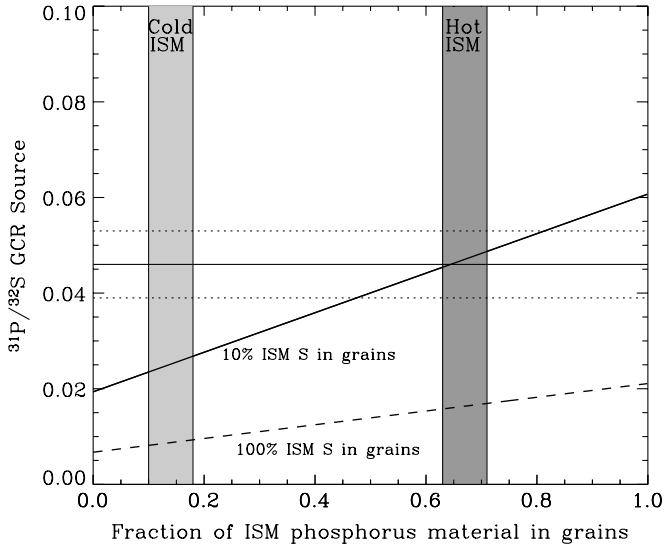

Figure 9. Superbubble $^{31}P/^{32}S$ ratio as a function of the interstellar P grain fraction, for a 10% and 100% fraction of interstellar S in grains. The derived GCR source $^{31}P/^{32}S$ ratio is plotted as a horizontal line, with dotted lines showing the uncertainty on this ratio. The hot and cold ISM band widths span the uncertainties given by Cartledge et al. (2006).

be 0.14 ± 0.04 in the cold ISM and 0.67 ± 0.04 in the hot ISM (Cartledge et al. 2006). If 100% of the interstellar sulfur is assumed to be in grains, the superbubble $^{31}P/^{32}S$ ratio is not consistent with the derived $^{31}P/^{32}S$ in the cosmic rays for any grain fraction of ISM phosphorus. However, if 10% of the interstellar sulfur is in grains, the superbubble $^{31}P/^{32}S$ ratio is consistent with the observed cosmic ray source ratio at the appropriate ISM phosphorus grain fraction for the hot ISM. The interstellar material near star-forming regions mixed into the superbubble core is hot, so a phosphorus grain fraction of ∼0.67 is appropriate for the GCR seed material. This material is much warmer than 30 K, so the 10% interstellar sulfur grain fraction is consistent with that derived in warmer environments by Goicoechea et al. (2006) and is inconsistent with a large sulfur depletion onto dust grains in the GCR source environment. It should be noted that there is an uncertainty on the derived superbubble abundances, though it is not clear how to obtain an estimate of it.

4.3.2. $^{38}Ar/^{36}Ar$, $^{44}Ca/^{40}Ca$, and $^{48}Ca/^{40}Ca$ at the GCR Source

The noble gas argon exists solely in the gas phase in the superbubble core. The expected $^{38}Ar/^{36}Ar$ ratio in the superbubble is calculated as the $^{34}S/^{32}S$ and $^{31}P/^{32}S$ ratios were calculated, and is found to be 0.203, which is about 1.1σ larger than the derived GCR source ratio (Table 6).

Calcium, a refractory element, exists almost entirely as grains in the interstellar medium (Jenkins 2004). The expected superbubble $^{44}Ca/^{40}Ca$ ratio is calculated to range from 0.0200 if the ejecta material is entirely gaseous, to 0.0156 if the ejecta is all dust. The GCR source $^{44}Ca/^{40}Ca$ ratio was derived to be 0.0195 with a large uncertainty of 0.0112, so it is not possible to constrain the amount of condensation of supernova grains with this ratio. Since calcium is refractory, the Ca ejecta grain fraction is equivalent to the supernova dust condensation efficiency. This is an important parameter that is relevant to other areas of astrophysics; constraining this parameter with other cosmic ray refractories could provide valuable insight into the galactic dust environment.

The $^{48}Ca/^{40}Ca$ GCR source ratio was determined with CRIS ^{48}Ca abundances by Wiedenbeck et al. (2001a). The neutron-rich, doubly magic isotope ^{48}Ca is almost entirely of primary origin in the cosmic rays, the secondary correction is small, so its source abundance can be derived to high accuracy. The $^{48}Ca/^{40}Ca$ GCR source ratio was determined to be 0.0024 ± 0.0002 (slightly higher than the Lodders 2003 solar system ratio of 0.0019). The calculation of the superbubble abundances of ^{48}Ca, and to a lesser degree ^{44}Ca, depends very sensitively

on the frequency and explosion details of Type Ia supernovae (Woosley et al. 1998). A superbubble $^{48}Ca/^{40}Ca$ ratio cannot be accurately determined given the uncertainty in the frequencies of different varieties of Type Ia supernovae inside a superbubble, so it is not possible to significantly constrain the supernova dust condensation efficiency from this ratio.

5. CONCLUSIONS

The cosmic ray $^{31}P/^{32}S$, $^{34}S/^{32}S$, $^{38}Ar/^{36}Ar$, and $^{44}Ca/^{40}Ca$ GCR source ratios were derived with sufficient accuracy to provide significant constraints on the cosmic ray source environment. The $^{31}P/^{32}S$ ratio strongly supports volatility over FIP as the mechanism of GCR fractionation. The $^{38}Ar/^{36}Ar$ and $^{44}Ca/^{40}Ca$ GCR source ratios are consistent with the superbubble origin of cosmic rays. From the $^{36}Ar/^{40}Ca$ ratio, the grain/gas efficiency factor was calculated to be 6.4 ± 0.3. The derived GCR source phosphorus and sulfur composition is in agreement with the superbubble origin if the P and S dust fractions of the interstellar material (which composes 80% of the GCR source environment) is consistent with recent astronomical observations of similar hot galactic environments: about 10% of the sulfur and about 67% of the phosphorus in grains, with the remainder in gas.

This work was supported by NASA at the California Institute of Technology (under grant NAG5-12929), the Jet Propulsion Laboratory, the Goddard Space Flight Center, and Washington University. I.V.M. acknowledges NASA and APRA grants for partial support.

REFERENCES

Arnett, W. D. 1978, in Proc. IAU Colloq. 45, Chemical and Dynamical Evolution of our Galaxy, ed. E. Basinka-Grzesik & M. Mayor (Sauverny, Switzerland: Geneva Observatory), 161
Arnould, M., Goriely, S., & Meynet, G. 2006, A&A, 453, 653
Binns, W. R., et al. 2000, in AIP Conf. Proc. 528, Acceleration and Transport of Energetic Particles Observed in the Heliosphere (Melville, NY: AIP), 413
Binns, W. R., et al. 2005, ApJ, 634, 351
Binns, W. R., et al. 2007, in Proc. 30th Int. Cosmic Ray Conf. (Merida), 2, 27
Bradley, J. P., et al. 1999, Science, 285, 1716B
Cartledge, S. I. B., Lauroesch, J. T., Meyer, D. M., & Sofia, U. J. 2006, ApJ, 641, 327
Cassé, M., & Goret, P. 1978, ApJ, 221, 703
Chin, Y. N., Henkel, C., Whiteoak, J. B., Langer, N., & Churchwell, E. B. 1996, A&A, 305, 960
Davis, A. J., et al. 2000, in AIP Conf. Proc. 528, Acceleration and Transport of Energetic Particles Observed in the Heliosphere (Melville, NY: AIP), 421
Ellison, D. C., Drury, L. O'C., & Meyer, J.-P. 1997, ApJ, 487, 197
Engelmann, J. J., et al. 1990, A&A, 233, 96
Ercolano, B., Barlow, M. J., & Sugerman, B. E. K. 2007, MNRAS, 375, 753E
Fisk, L. A. 1971, J. Geophys. Res., 76, 221
Fryer, C. L. 1999, ApJ, 522, 413
George, J. S., et al. 2001, in AIP Conf. Proc. 598, Joint *SOHO*/ACE Workshop, Solar and Galactic Composition, ed. R. F. Wimmer-Schweingruber (Melville, NY: AIP), 263
George, J. S., et al. 2009, ApJ, in press
Goicoechea, J. R., Pety, J., Gerin, M., Teyssier, D., Roueff, E., Hily-Blant, P., & Baek, S. 2006, A&A, 456, 565G
Hatano, K., Fisher, A., & Branch, D. 1997, MNRAS, 290, 360
Heger, A., et al. 2003, ApJ, 591, 288
Higdon, J. C., & Lingenfelter, R. E. 2003, ApJ, 590, 822
Higdon, J. C., Lingenfelter, R. E., & Ramaty, R. 1998, ApJ, 509, L33
Hinshaw, G. F., & Wiedenbeck, M. E. 1983, in Proc. 18th Int. Cosmic Ray Conf. (Bangalore), 9, 263
Howk, J. C., Sembach, K. R., & Savage, B. D. 2006, ApJ, 637, 333
Iwamoto, K., Brachwitz, F., Nomoto, K., Kishimoto, N., Umeda, H., Hix, W. R., & Thielemann, F. 1999, ApJS, 125, 439
Jansen, D. J., Van Dishoeck, E. F., & Black, J. H. 1994, A&A, 282, 605
Jenkins, E. B. 2004, in Origin and Evolution of the Elements, ed. A. McWilliams & M. Rauch (Cambridge: Cambridge Univ. Press), 336 (arXiv:astro-ph/0309651)
Lingenfelter, R. E., & Higdon, J. C. 2007, ApJ, 660, 330L
Lodders, K. 2003, ApJ, 159, 1220
Massey, P., et al. 1995, ApJ, 454, 151
Meneguzzi, M., Audouze, J., & Reeves, H. 1971, A&A, 15, 337
Meyer, J.-P. 1985, ApJS, 57, 173
Meyer, J.-P., Drury, L. O'C., & Ellison, D. C. 1997, ApJ, 487, 182
Meynet, G., Arnould, M., Paulus, G., & Maeder, A. 2001, Space Sci. Rev., 99, 73
Meynet, G., & Maeder, A. 2005, A&A, 429, 581
Millar, T. J., & Herbst, E. 1990, A&A, 231, 466
Moskalenko, I. V., Strong, A. W., & Porter, T. A. 2007, in Proc. 30th Int.Cosmic Ray Conf. (Merida), 2, 129
Ogliore, R. C. 2007, PhD thesis, California Institute of Technology
Orear, J. 1982, Notes on Statistics for Physicists, Revised (Ithaca, NY: Cornell Univ.)
Raisbeck, G. M. 1979, in Proc. 16th Int. Cosmic Ray Conf. (Paris), 14, 146
Rauscher, T., Heger, A., Hoffman, R. D., & Woosley, S. E. 2002, ApJ, 576, 233
Salpeter, E. E. 1955, ApJ, 121, 161
Savage, B. D., & Sembach, K. R. 1996, ARA&A, 34, 279
Schaller, G., Schaerer, D., Meynet, G., & Maeder, A. 1992, A&AS, 96, 269
Snow, T. P., & Witt, A. N. 1996, ApJ, 468, L65
Stone, E. C., & Wiedenbeck, M. E. 1979, ApJ, 231, 606
Stone, E. C., et al. 1998, Space Sci. Rev., 86, 285
Streitmatter, R. E., et al. 1985, A&A, 143, 249
Strong, A. W., Moskalenko, I. V., & Ptuskin, V. S. 2007, Ann. Rev. Nucl. Part. Sci., 57, 285
Tarafdar, S. P., & Apparao, K. M. V. 1981, Ap&SS, 77, 521
Thayer, M. R. 1997, ApJ, 482, 792
Tieftrunk, A., Pineau des Forets, G., Schilke, P., & Walmsley, C. M. 1994, A&A, 289, 579
van den Bergh, S., & McClure, R. D. 1994, ApJ, 425, 205
Villagrasa-Canton, C., et al. 2007, Phys. Rev. C., 75, 044603
Webber, W. R., et al. 1990, Phys. Rev. C, 41, 566
Westphal, A. J., & Bradley, J. P. 2004, ApJ, 617, 1131
Wiedenbeck, M. E., et al. 2001a, in Proc. 27th Int. Cosmic Ray Conf. (Hamburg), 5, 1679
Wiedenbeck, M. E., et al. 2001b, Space Sci. Rev., 99, 15
Wiedenbeck, M. E., et al. 2005, in Proc. 29th Int. Cosmic Ray Conf. (Pune), 2, 277
Wiedenbeck, M. E., et al. 2007a, Space Sci. Rev., 130, 415
Wiedenbeck, M. E., et al. 2007b, in Proc. 30th Int. Cosmic Ray Conf. (Merida), 2, 149
Woosley, S. E., Hoffman, R. D., Timmes, F. X., Weaver, T. A., & Thielemann, F. K. 1998, Nucl. Phys. A, 621, 445
Woosley, S. E., Langer, N., & Weaver, T. A. 1995, ApJ, 448, 315
Woosley, S. E., & Weaver, T. A. 1995, ApJS, 101, 181
Yanasak, N. E., et al. 2001, ApJ, 563, 768